

# Eigenfeatures: Discrimination of X-ray images of epoxy resins using singular value decomposition of deep learning features

Edgar Avalos, Kazuto Akagi and Yasumasa Nishiura<sup>1</sup>

Mathematical Science Group, WPI-Advanced Institute for Materials Research (AIMR),  
Tohoku University, Japan

<sup>1</sup>Research Institute for Electronic Sciences, Hokkaido University and MathAM-OIL,  
Tohoku University and AIST, Japan

May 17, 2022

## Abstract

Although the process variables of epoxy resins alter their mechanical properties, the visual identification of the characteristic features of X-ray images of samples of these materials is challenging. To facilitate the identification, we approximate the magnitude of the gradient of the intensity field of the X-ray images of different kinds of epoxy resins and then we use deep learning to discover the most representative features of the transformed images. In this solution of the inverse problem to find characteristic features to discriminate samples of heterogeneous materials, we use the eigenvectors obtained from the singular value decomposition of all the channels of the feature maps of the early layers in a convolutional neural network. While the strongest activated channel gives a visual representation of the characteristic features, often these are not robust enough in some practical settings. On the other hand, the left singular vectors of the matrix decomposition of the feature maps, barely change when variables such as the capacity of the network or network architecture change. High classification accuracy and robustness of characteristic features are presented in this work.

## 1 Introduction

X-ray CT imaging of polymer composites enables the non-destructive visualization of three-dimensional samples as well as two-dimensional slices of the material [1]. Despite the significant improvements in the spatial resolution, the resulting images exhibit highly fluctuating electron density patterns that are extremely difficult to discriminate by simple observation.

The problem of grouping images of samples of materials with similar properties was recently addressed [2]. However, while it is possible to categorize X-ray images with similar properties, the associated inverse problem of finding out what are the most relevant features in the images that differentiate samples from one another, remains unsolved. In this paper we propose a solution based on deep learning to the inverse problem.

Machine learning tools are widely used to identify and categorize different samples of materials and to predict their properties [3, 4, 5]. Some examples include deep convolutional neural networks (CNN) [6, 7] that are highly accurate to classify images by minimizing a suitable cost function [8]. By visualizing the intermediate responses in a CNN one can have a better understanding of the features that the net uses for classification [9, 10]. Among some few applications that take advantage of this approach, we can mention Ref. [11], in which the authors use a CNN that is able not only to classify crystals with astonishing accuracy, but remarkably the activated filters of the early layers produce visual fingerprints that distinguish among different crystal symmetries. Similarly in Ref. [12], the authors use a CNN to analyze thermal images by looking at

the strongest activation channel of the intermediate layers to construct a visual representation of the early signs of failure in power transformers. In another impressive application, Lakhani et al. [11] are able to visualize features on the intermediate layers in a CNN to detect pulmonary tuberculosis on chest radiographs. An additional example illustrates the use of the activations of the early layers to highlight driver behaviours [13].

The singular value decomposition (SVD) of a matrix  $A$  representing a collection of images, provides with an orthonormal basis that can be used to describe correlations between individual images in  $A$ . We use SVD to discover the features in X-ray images that are relevant for classification. Although SVD has been used to improve the training of neural networks [14, 15, 16], to the best of our knowledge, the analysis of the statistical correlations of the feature maps in the early layers of a CNN has not been utilized to discriminate X-ray images of samples of epoxy resins.

## 2 Methods

### 2.1 Materials and image acquisition

We consider X-ray CT images of four different samples of thermosetting resins as shown in figure 1. The samples 1 to 4 used in our analysis have the same chemical composition of bisphenol A type epoxy molecule and hardener molecule (primary diamine) with a ratio 3:1. Different conditions of heating temperature and heating time endow the samples with different mechanical properties. Additionally, as it can be seen in figure 1, different processing conditions also result in different patterns of density in the X-ray images. However, the differences are not evident by simple observation. The goal is to identify the characteristic features in the samples that are relevant for their classification.

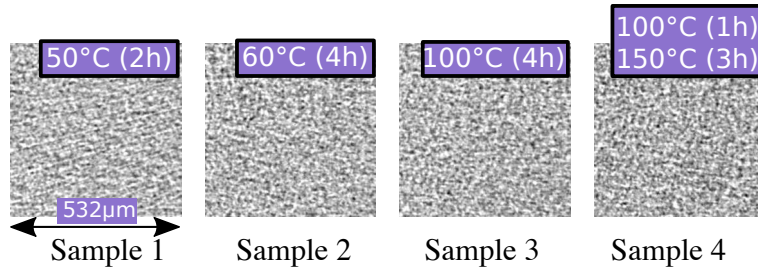


Figure 1: X-ray CT images of four samples of epoxy resins. Variations of the process variables, such as heating and heating time, produce different patterns of density in the X-ray images.

The samples were prepared as a plate with a thickness of 1mm and their mechanical properties were measured by the standard means of evaluation. The polymerization rate, density and fracture toughness are summarized in Table 1. The X-ray CT images were obtained using a commercial apparatus with the resolution of  $2 \mu\text{m}/\text{pixel}$  by NIPPON STEEL Chemical & Material CO., LTD. Two squared sections of size  $266 \times 266$  pixels were cut out from left and right sides of the plate, which were then sampled into X-ray images using 266 slices every  $2 \mu\text{m}$  (Figure 2). In a X-ray CT image, the bright part corresponds to high electron density ( $\equiv$  high atomic density) part. Since the three-dimensional network of covalent bonds obstructs the packing of molecules, we assume that highly polymerized part corresponds to low density (dark) part. On the other hand, highly polymerized part has larger Young's modulus, therefore, dark part is considered to have larger Young's modulus than bright one.

Table 1: Properties of the samples (provided by NIPPON STEEL Chemical & Material CO., LTD.)

	Sample 1	Sample 2	Sample 3	Sample 4
Polymerization Rate [%]	13.7	45.9	60.3	90.0
Density [ $g/cm^3$ ]	1.151	1.157	1.145	1.143
Fracture Toughness [ $MPa \cdot m^{1/2}$ ]	0.16	1.03	0.99	0.83

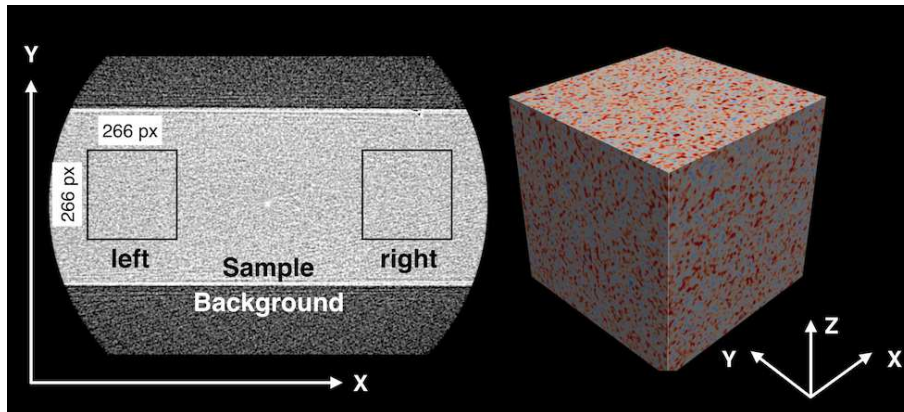


Figure 2: (Color online)(Left) An example of X-ray CT slice image. The middle bright area corresponds to the sample. The upper and lower dark background area shows a noisy image originated from the fluctuation of X-ray intensity. (Right) 3D reconstruction using 266 slices. The brighter (darker) parts are colored red (blue).

## 2.2 Preprocessing

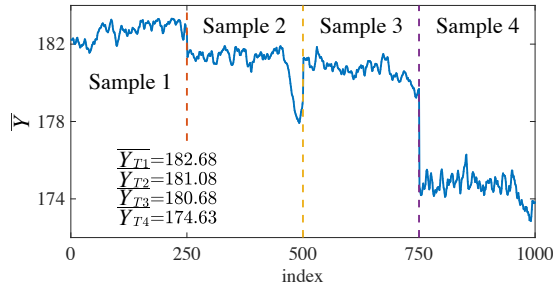
### 2.2.1 Basic statistical quantities.

We look into some basic statistical parameters in the set of the X-ray images. To analyze the distribution of the pixel values in the X-ray images, we proceed as follows. For each grayscale X-ray image with pixels taking values between 0 and 255, we compute the mean value in a fixed squared domain ( $266 \times 266$ ). The total intensity of the images divided by the pixel count corresponds to the mean value of the images. Figure 3a shows the mean value of all the slices of samples 1 to 4. Figure 3b shows the mean of the module of the gradient of each slice computed as  $\frac{1}{N} \int (f_x^2 + f_y^2)^{1/2} dx dy$ , with  $N$  being the pixel count. Notice that sample No. 3 has the largest average value of the module of the gradient.

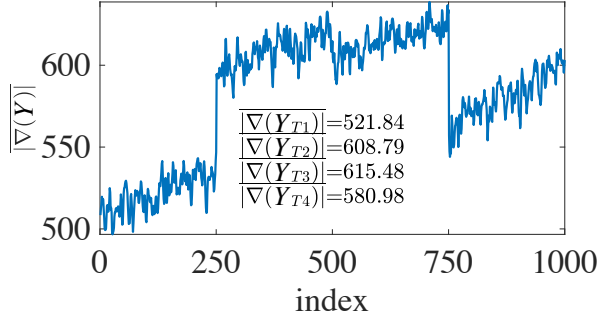
### 2.2.2 Robust gradient approximation

The original X-ray images describe the intensity field contain large fluctuations of intensity and it is required to remove all unnecessary information from the images. Previously, it has been shown that the adequate means to highlight the features of the X-ray images is to transform the intensity field into the module of the gradient of the images. One important reason to use this transformation is because the total variation of the images defined as the summation of all the local contributions of the module of the gradient, is a quantity related to the mechanical performance of the samples [2]. This choice is additionally strengthened by the fact that the module of the gradient produces the correct classification of the images, which places the sample No. 3 as the one with the best mechanical performance [2].

To compute the module of the gradient we process as follows. For each image  $Y$  defined as a  $m \times n$  array, we need to compute the derivatives in the horizontal and vertical directions,  $\frac{\partial Y}{\partial x}$



(a) Mean of each slice.



(b) Module of the gradient

Figure 3: (Color online) (a) Mean value of the intensity field of each X-ray image shown as  $\overline{Y_{S_i}}$ . The index number represents each image and it runs from 1 to 1064. From left to right, the vertical lines separate samples 1 to 4. (b) Mean of the module of the gradient of each slice,  $\frac{1}{N} \int (f_x^2 + f_y^2)^{1/2} dx dy$ , with  $N$  being the pixel count. Sample No. 3 has the largest average value of the module of the gradient.

and  $\frac{\partial Y}{\partial y}$ , respectively. The module of the gradient is then defined as

$$\nabla Y = \begin{bmatrix} Y_x \\ Y_y \end{bmatrix} = \begin{bmatrix} \frac{\partial Y}{\partial x} \\ \frac{\partial Y}{\partial y} \end{bmatrix} \quad (1)$$

$$|\nabla Y| = \sqrt{Y_x^2 + Y_y^2}, \quad (2)$$

where  $Y_x$  and  $Y_y$  represent simple discrete approximations of the forward difference for interior data points in the horizontal and vertical direction, respectively. For example, for a matrix with unit-spaced data,  $Y$ , that has vertical gradient,  $Y_x$ , the interior gradient values are computed as  $(f_{i,j+1} - f_{i,j})$ . The horizontal gradient is computed similarly.

The calculation of the module of the gradient of each image  $Y$  shows that he transformed image  $|\nabla Y|$  reveals previously unseen worm-like fibers. (See Figure 5). Additionally, it is well-known that noise suppression is an important issue when dealing with derivatives to compute the gradient [17]. Therefore the discretization of the gradient function requires special attention. Although simple algorithms of differentiation such as central difference and forward difference produce good results of clustering [2], these methods are not longer satisfactory to visualize the gradient of an image with noisy background. A more comprehensive computation of the gradient is necessary to capture a richer content of visual details in the image of  $|\nabla Y|$ .

In addition to forward differences, there are other methods to approximate the gradient. More in general, the gradient of a given image  $Y$  is computed through a 2D convolution with a  $3 \times 3$  mask  $Z$ , as shown in Eqn. 3.

$$C(x, y) = \sum_{t=-1}^1 \sum_{s=-1}^1 Z(s, t) Y(x - s, y - t) \quad (3)$$

Figure 4 shows several masks to perform the approximation of the derivatives needed for the gradient operator. While the forward difference approximation (Figure 4b) preserves clusters in an eigenspace [2], the contribution of additional neighbouring locations improves the gradient approximation. Prewitt mask shown in Figure 4c, produces a more comprehensive value of the gradient that includes neighbouring contributions of a given location. Additionally, the Sobel mask shown in Figure 4d gives more weight to the central pixel. Sobel masks have better noise-suppression (smoothing) characteristics [17].

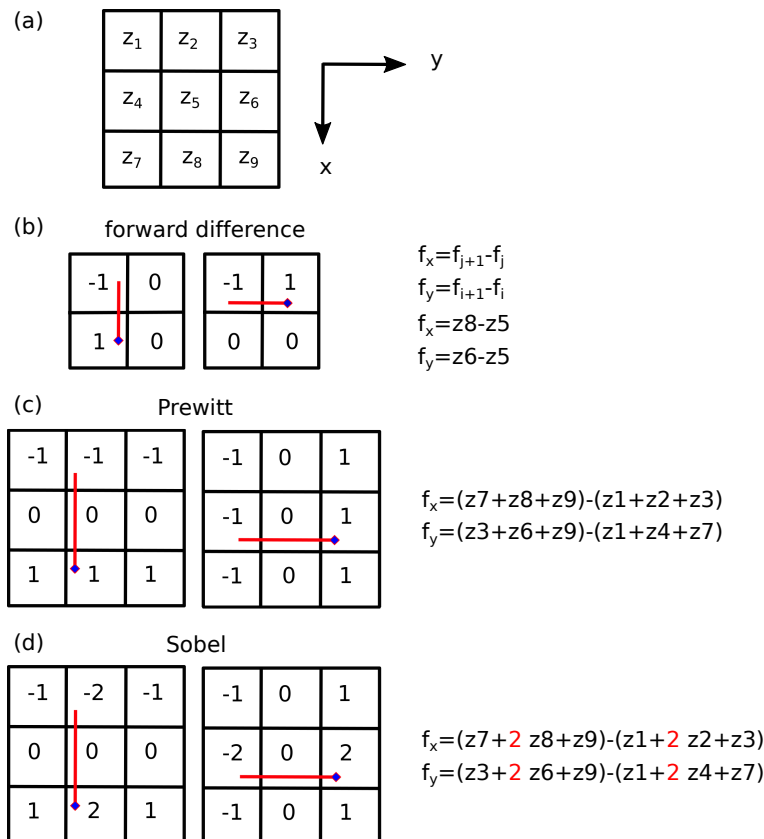


Figure 4: Filter masks to compute the derivatives needed for the gradient operator. (a) Generic  $3 \times 3$  mask with the ordering of its elements shown as  $z_p$ , with  $p = 1, \dots, 9$ . (b) Simple forward approximation. (c) Prewitt mask. (d) Sobel mask. Notice this mask gives twice the weight to the central pixel compared to Prewitt.

As a visual example, Figure 5 shows  $|\nabla Y|$  for a typical image of sample 1 computed using forward difference and a Sobel mask. Notice that additional details are captured by the Sobel mask. In what follows, we use the Sobel operator to transform the intensity field of the whole set of X-ray images into the corresponding absolute gradient field. The goal is to discover the most notable features that are relevant to classify the images.

## 2.3 Convolutional neural network

### 2.3.1 Architecture description

A CNN is a type of neural network [18, 19] that uses convolution (Eqn. 4) to process 2D numerical arrays such as images. Figure 7 shows a schematic representation of the CNN used in this work. The CNN is composed of several convolutional blocks including convolution, batch normalization, rectified linear unit (ReLU) and MaxPooling. The final end of the CNN consists of one fully-connected layer and one Softmax layer. The two-dimensional convolution of the input  $Y$  with a



(a)  $|\nabla Y|$  computed used forward difference. (b)  $|\nabla Y|$  computed used a Sobel mask.

Figure 5: Image of module of gradient of sample 1 using two different approximation methods.

kernel  $W$ , denoted as  $C(m, n) = Y(m, n) * W(m, n)$ , is defined as

$$C(m, n) = \sum_{t=-\infty}^{\infty} \sum_{s=-\infty}^{\infty} W(s, t) Y(x - s, y - t) \quad (4)$$

Where  $m$  and  $n$  are indices along the horizontal and vertical directions, respectively. The resulting function  $C(m, n)$  is the output or feature map of the convolution. For a given image  $y_i$  at the  $l$ -th layer, the convolution produces the output

$$s_j^l = f\left(y_i^{l-1} * w_{ij}^l + b_j^l\right) \quad (5)$$

Where  $w_{ij}^l$  are learnable parameters,  $b_j^l$  is a bias and  $f(\cdot)$  is the output of the activation function [20]. To normalize the activations of the convolution,  $x_i$ , we use batch normalization [21] with a mini-batch mean  $\mu_B$  and standard deviation  $\sigma_B^2$  as:

$$\hat{x}_i = \frac{x_i - \mu_B}{\sqrt{\sigma_B^2 + \epsilon}} \quad (6)$$

A small value of  $\epsilon$  is needed in case the mini-batch variance is very small. The rectified linear unit (ReLU) defined in Eqn. 7 [22, 23], is employed as nonlinear activation function because it is faster than other alternatives such as the sigmoid or  $\tanh(\cdot)$  functions. What the ReLU function does is to clip the negative part out of the output of the activations of the convolution.

$$g(z) = \max(0, z) \quad (7)$$

Maxpooling is employed on the activations after the ReLU function to down-sample the spatial size of the input arrays by taking the maximum values of a subset of the input array [24].

Five convolutional blocks are employed in sequence and then the fully connected layer executes a linear combination of the features of the output of the previous layer

$$h_j^l = f\left(\sum_i \left(x_i^{l-1} w_{ij}^l\right) + b_j^l\right) \quad (8)$$

In this case  $l$  denotes the  $l$ -th layer,  $b_j$  is a given bias,  $w_{ij}$  is the  $ij$ -th weight between the input  $x_i$  and the  $j$ -th output unit  $h_j$ . In our case  $j = 1, 2, 3$ , and 4. To normalize the output of the fully connected layer in the range  $[0, 1]$ , we use the softmax function (Eqn. 9). The

values of  $\text{softmax}(z)_i$  represent probabilities of the classes  $i = 1, 2, 3$ , and 4. The total sum of the probabilities of the four classes is 1.

$$\text{softmax}(z)_i = \frac{e^{z_i}}{\sum_j e^{z_j}} \quad (9)$$

We initialize the training with random values of the weights and then run the entire data set of images for several epochs. The classification error for multiple samples and multiple classes is computed using cross-entropy as loss function,  $J$ , as

$$J = - \sum_{i=1}^N \sum_{j=1}^K t_{ij} \ln y_{ij} \quad (10)$$

Where  $t_{ji}$  indicates the  $i$ -th image belongs to the  $j$ -th class and  $y_{ij}$  is the  $i$ -th prediction obtained for class  $j$  from the softmax activation (Eqn. 9). We want to minimize the cost function with respect to all the parameters  $w_{ij}^l$  in the model as

$$\arg \min_{w_{ij}^l} J \quad (11)$$

The architecture of the convolutional neural network used in this work is detailed in Table 1.

Training was performed using stochastic gradient descent [25] to minimize the loss function (Eqn. 10) in such a way that both the weights of both the convolutional and fully-connected layers are updated to reduce the error. To evaluate the gradient of the loss function and update the weights, we use batches of 64 images and a learning rate is set equal to  $10^{-2}$ . The validation frequency is equal to five iterations. Using these values, the classification error steadily decreases to its smallest value. Recent results show that mini-batches of small size work improved training performance and allow a significantly smaller memory footprint [26, 27]. We confirmed that using a mini-batch of size 32 or 64 produces similar feature maps. To prevent overfitting, we have employed a dropout layer [28] at the fully connected layer to randomly set input elements to zero with a given probability of 0.5. Adding a  $\ell_2$ -regularization term for the weights to the loss function also helps to reduce overfitting [29, 30]. The loss function with the regularization term takes the form

$$J_R = J + \lambda \Omega(w) \quad (12)$$

Where  $w$  is the weight vector,  $\lambda = 0.1$  is the regularization factor and  $\Omega(w) = \frac{1}{2} \|w\|^2 = \frac{1}{2} w^T w$ . Dropout combined with  $\ell_2$ -regularization gives a lower classification error [28].

**IMAGE PREPROCESSING AND TRAINING PROCEDURE.** We use grayscale 8-bit images with pixel intensities taking values from 0 to 255. The set of input images consist of 1064 image files stored in a TIF format with the resolution of  $266 \times 266$  pixels. To have the data dimensions of approximately the same scale, we use normalize the images by dividing each image by its standard deviation once it has been zero-centered. Zero-centering means subtracting the mean from each image. Data augmentation is a powerful method to reduce both the validation and training errors by artificially in enlarge the training dataset size by data warping. The augmented data represents a more comprehensive set of possible data points, thus minimizing the distance between the training and validation set [31]. We employ mirror and upside-down transformations to expand our data base. The images were grouped in four sets, each with 266 images and labels of four classes were assigned to all the images. For each epoch the training set was randomly divided into 2 groups, one data set with 70% of the images for training and the reminding 30% for validation. The validation data is shuffled before each network validation. Over 98% Cross-validation accuracy was achieved. Figure 6 shows the training progress. The network was trained using a CUDA enabled Nvidia Quadro GP100 GPU.

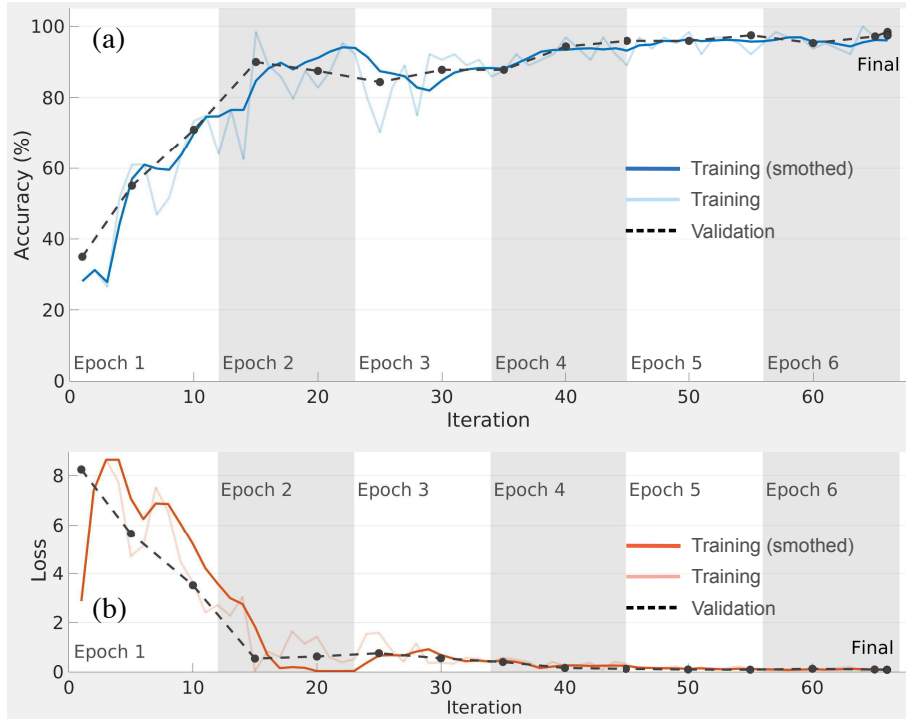


Figure 6: Training progress of the CNN using the hyperparameters described in the text. Using a mini-batch size of 64, it takes 11 iterations to all of the training samples pass through the learning algorithm. (a) Training and validation accuracy reaches more or less the same high values after 60 iterations. (b) The steady decrease of the training and validation loss functions suggests that there is not significant overfitting.

## 3 Results

### 3.1 Inverse problem

The inverse problem consists in finding features in the X-ray images that distinguish different samples of material. To solve this problem we choose to employ a CNN because these computing systems are able to classify images with high accuracy [10, 32]. We want to analyze the most representative features that a CNN uses to classify X-ray images. Although CNN’s typically achieve a high accuracy in classification, a deep learning solution to the inverse problem is not easy to interpret because the number of parameters involved in the classification process is of the order of millions. However a simple approach is to look at the early layers in the network. The filters in the first few layers of a CNN are relatively easy to understand as their primary purpose is to detect edges in the images. These edges and other low level features at the early layers of a CNN describe regions in the images that are important for classification. The loadings of the filters of a CNN are learnable parameters that are optimized during the training process for classification. In this section, firstly we train a CNN to classify the transformed images and secondly we extract the learned features at the early layers of the net. The schematics of the net used in this work is shown in figure 7 and the details of each layer are shown in Table 2.

A simple idea to address the inverse problem is to feed a gradient image  $|\nabla Y|$  into a trained CNN and then look at the responses at the early layers [10]. The hope is that such responses reveal the presence of edges in the form of gradients of intensity. These responses at the early layers of a CNN show lumps or spots where the gradient is large. These regions are important for classification.

Table 2:

Architecture of the convolutional neural network	
Layer type	Specification
Convolutional layer	(Kernel: $3 \times 3$ ; 128 filters)
ReLU	
Max pooling layer	(Pool size: $2 \times 2$ ; stride: $2 \times 2$ )
Convolutional layer	(Kernel: $5 \times 5$ ; 128 filters)
ReLU	
Max pooling layer	(Pool size: $2 \times 2$ ; stride: $2 \times 2$ )
Convolutional layer	(Kernel: $7 \times 7$ ; 64 filters)
ReLU	
Max pooling layer	(Pool size: $2 \times 2$ ; stride: $2 \times 2$ )
Convolutional layer	(Kernel: $9 \times 9$ ; 64 filters)
ReLU	
Max pooling layer	(Pool size: $2 \times 2$ ; stride: $2 \times 2$ )
Convolutional layer	(Kernel: $11 \times 11$ ; 64 filters)
ReLU	
Max pooling layer	(Pool size: $2 \times 2$ ; stride: $2 \times 2$ )
Fully connected layer	(size: 4)
Softmax	

### 3.2 Response maps of a convolutional neural network

We examine the responses of different layers of the network summarized in figure 7 and discover which features the network learns by comparing areas of activation with the original image. Channels in early layers learn simple features like edges, while channels in the deeper layers learn complex features. We focus only on the early layers of the network.

We consider the first two layers in a CNN, namely, Conv1 and Conv2. Each layer consists of  $3 \times 3$  and  $5 \times 5$  filters, respectively, and each of these two layers contains 128 channels or feature maps. Activation functions placed after each convolutional layer, are responsible for transforming the summed weighted input from the node into the activation of the node. We use the Rectified Linear Unit (ReLU) as activation function. Convolutional layers Conv1 and Conv2 are followed by activation functions ReLU1 and ReLU2, respectively. Each channel in the convolutional layers encodes different features. For instance, they may encode diagonal or horizontal edges. Figure 8 shows all the features maps at the second layer. It is necessary to select a channel that illustrates the learned features at this layer and a common choice is the channel with the strongest activation [33, 34, 13]. This figure contains 128 features maps arranged in a  $12 \times 11$  array. The last four squares are empty. Each image in the array appears too dark and to improve the contrast we have stretched the range of intensity values of each image to span a desired range. We are saturating the upper 1% and the lower 1% of all pixel values. This enhancement is only for visualization purposes. For the calculations we employ the original intensity values of each feature map.

To select the channel with the strongest activation we iteratively search for the strongest activation among all the features maps in the responses at a particular layer. For two-dimensional response maps of size  $m \times n$  and  $k$  channels, the strongest channel is identified with index  $\alpha$  is obtained as follows:

$$\alpha = \max(f(x, y, l) : x \in 1..m, y \in 1..n, l = 1..k) \quad (13)$$

The figure 9, on the right hand side, shows from top to bottom the channel with the strongest activation,  $\alpha$ , at Conv1, Conv2 and ReLU2, respectively. The left hand side in all cases is the image of the absolute gradient  $|\nabla Y|$ . To simplify the notation we will refer to this quantity as  $X = |\nabla Y|$ . Notice that the responses at Conv1 look quite similar to the original image of  $X$ ,

which means that Conv1 is fundamentally acquiring the basic shape of the features in the images.

Conv2 learns features that are slightly larger in size than those in Conv1, because the filters in Conv2 are slightly larger than those in Conv1 as well. Notice that Conv2 reveals zones where the concentration of  $X$  is large. These zones contains lumps of intensity that can be more easily seen at the activation function of Conv2, which is called ReLU2. The ReLU function simply clips any negative activation from the output of the second convolutional layer.

The bottom row in Figure 9 shows a comparison of the original image of  $X$  and the  $\alpha$  channel at ReLU2. The bright lumps highlight zones of large concentration of  $X$ . One can repeat this process for the whole set of the X-ray images and then compute the mean value of the activations. The result is shown in Figure 10. This figure shows the mean value of the  $\alpha$  channel at ReLU1 and ReLU2. Notice that the ordering of these responses agrees with what was found in Ref. [2], as expected. In other words, the mechanical performance is high in materials with large concentration of the magnitude of the gradient.

Figure 11 is a solution to the inverse problem. Features in samples 1-4 can be easily distinguished by eye. Notice that sample No. 3 contains large concentration of activations. In this figure we employed an augmented data base of images, which is constructed by mirror and upside-down reflections on the horizontal and vertical directions, respectively. Using an augmented data base artificially enlarges the training set producing a clearer distinction of the learned features.

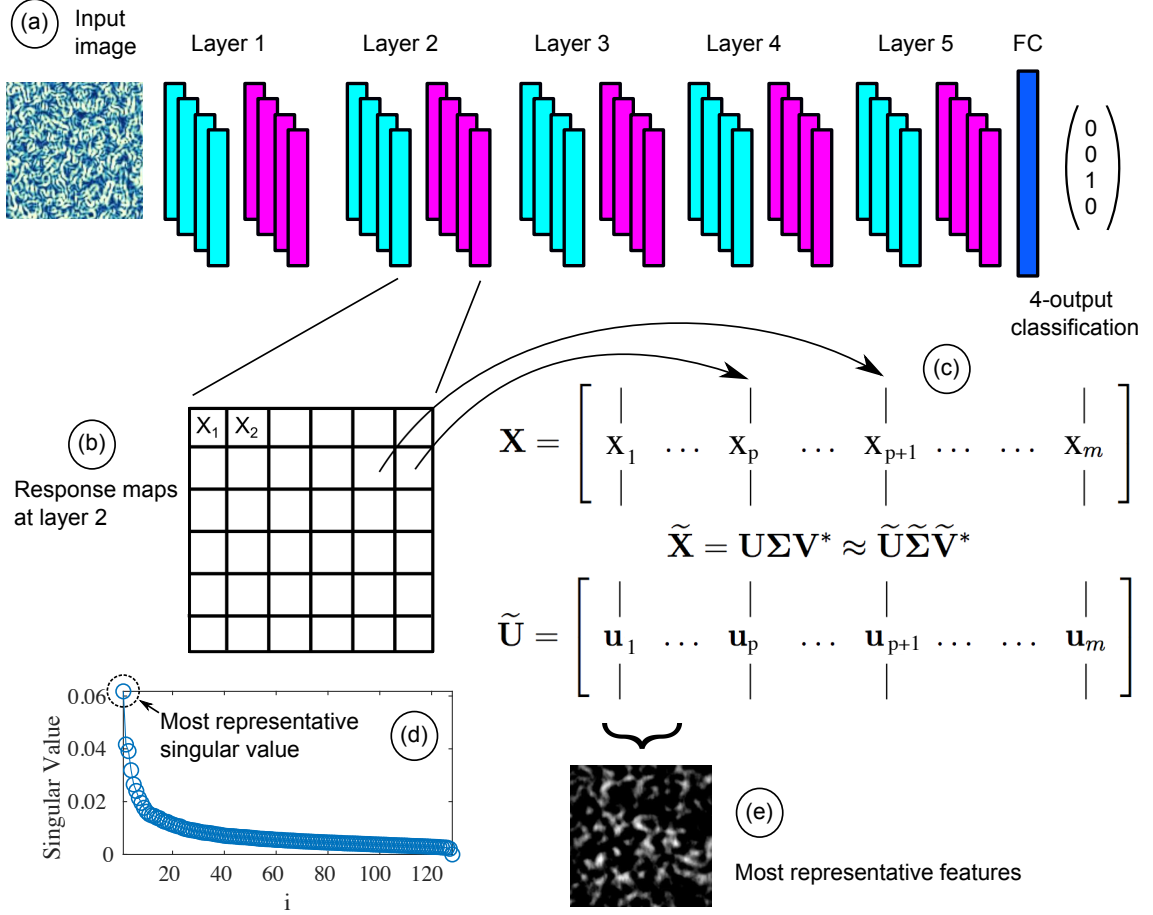


Figure 7: Schematics of the CNN used in this work. (a) An absolute gradient image  $|\nabla Y|$  is the input to a CNN with five layers. Each convolutional block consists of convolution, max-pooling and relu. A fully-connected layer with four outputs at the end. (b) The second convolutional layer contains 128 channels of response maps. Each response map  $X_i$  arranged as a column vector goes into a matrix  $\mathbf{X}$ . (c) SVD of  $\mathbf{X}$  produces a left singular eigenvector  $\mathbf{U}$  whose first column  $\mathbf{u}_1$  contains the most representative features of  $\mathbf{X}$ . (d) The fast decay of the singular values indicates that  $\mathbf{X}$  has its larger correlation along the  $\mathbf{u}_1$  eigendirection. Singular values are obtained from the singular value decomposition of the matrix  $\mathbf{X}$ . (e) The first eigenvector  $\mathbf{u}_1$  reshaped into an image of size equal to a response map represents the eigenfeatures of the input image.

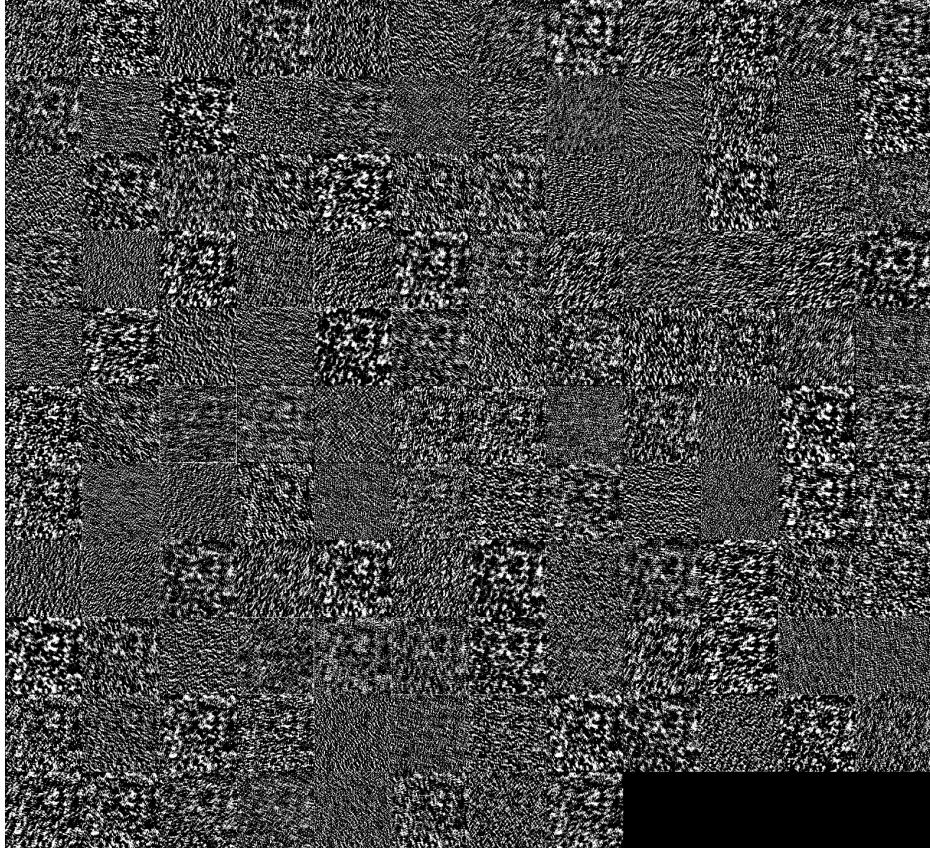


Figure 8: Response maps of the 128 channels in the second convolutional layer. The channels are the response to the classification process of a typical image of sample No. 3. The responses at ReLU2 are shown. For visualization purposes, the 2% of all pixel values have been saturated. For the calculations, we employ the original intensity values of each feature map. The features maps are arranged in a  $12 \times 11$  array. The last four squares at the bottom are empty.

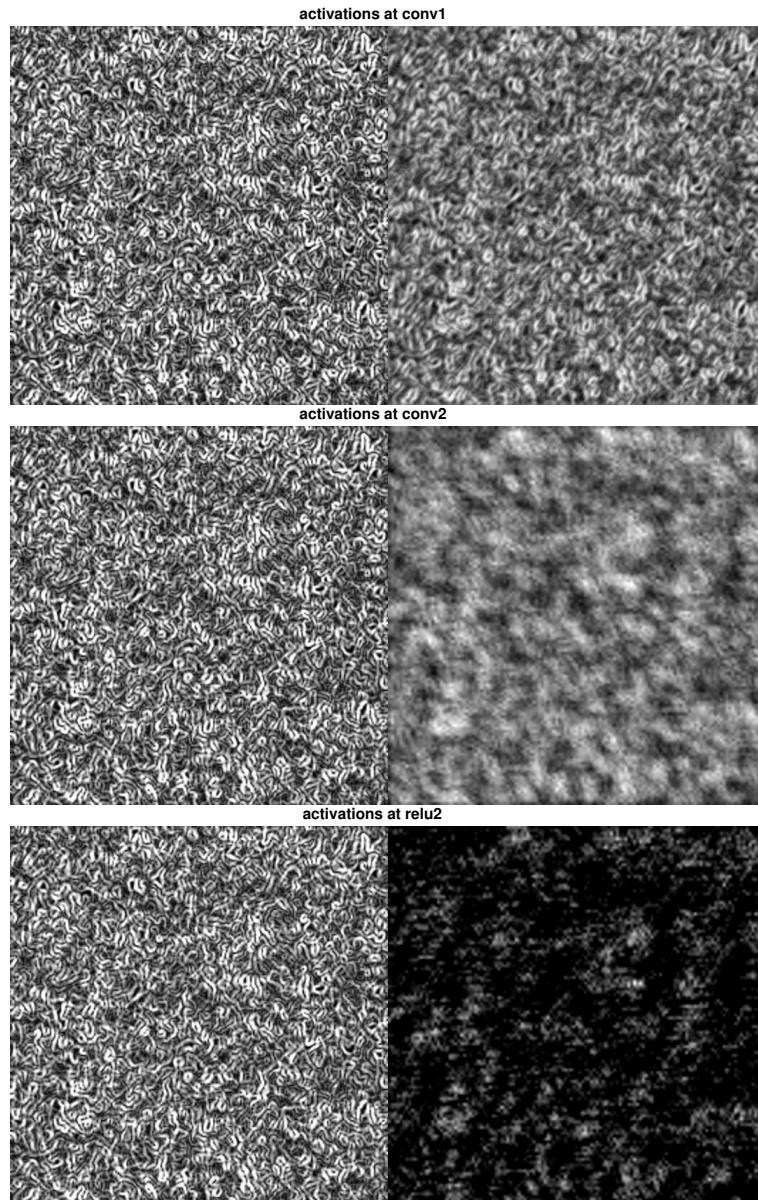
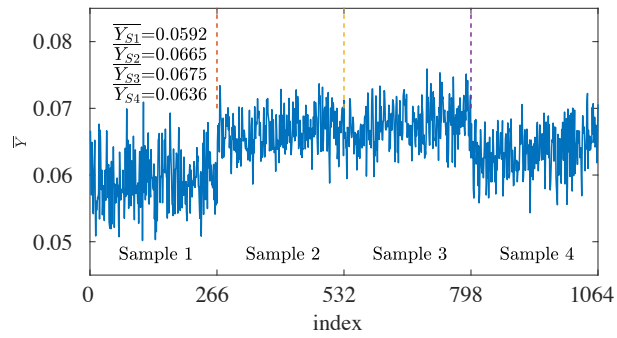
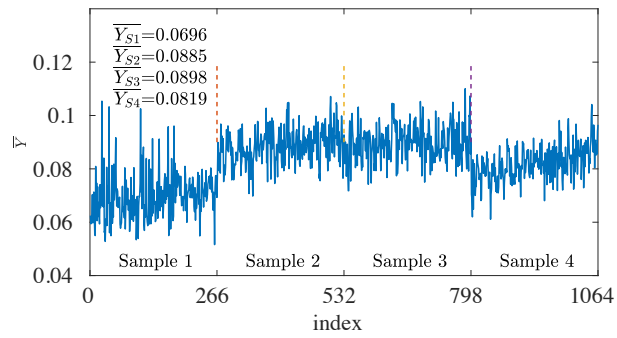


Figure 9: Comparison of the original image of  $X = |\nabla Y|$  (left hand side) and the strongest activation channel in different layers of the network for an image of sample No. 3 (right hand side). From top to bottom, the responses at layers Conv1, Conv2 and ReLU2, respectively.



(a) Mean value of activations at ReLU1



(b) Mean value of activations at ReLU2

Figure 10: Average values of the positive activations at the first (top) and second (bottom) convolutional layers. Notice that (i) the average values have the same ordering in both layers and that (ii) sample No. 3 has the largest average value in both layers.

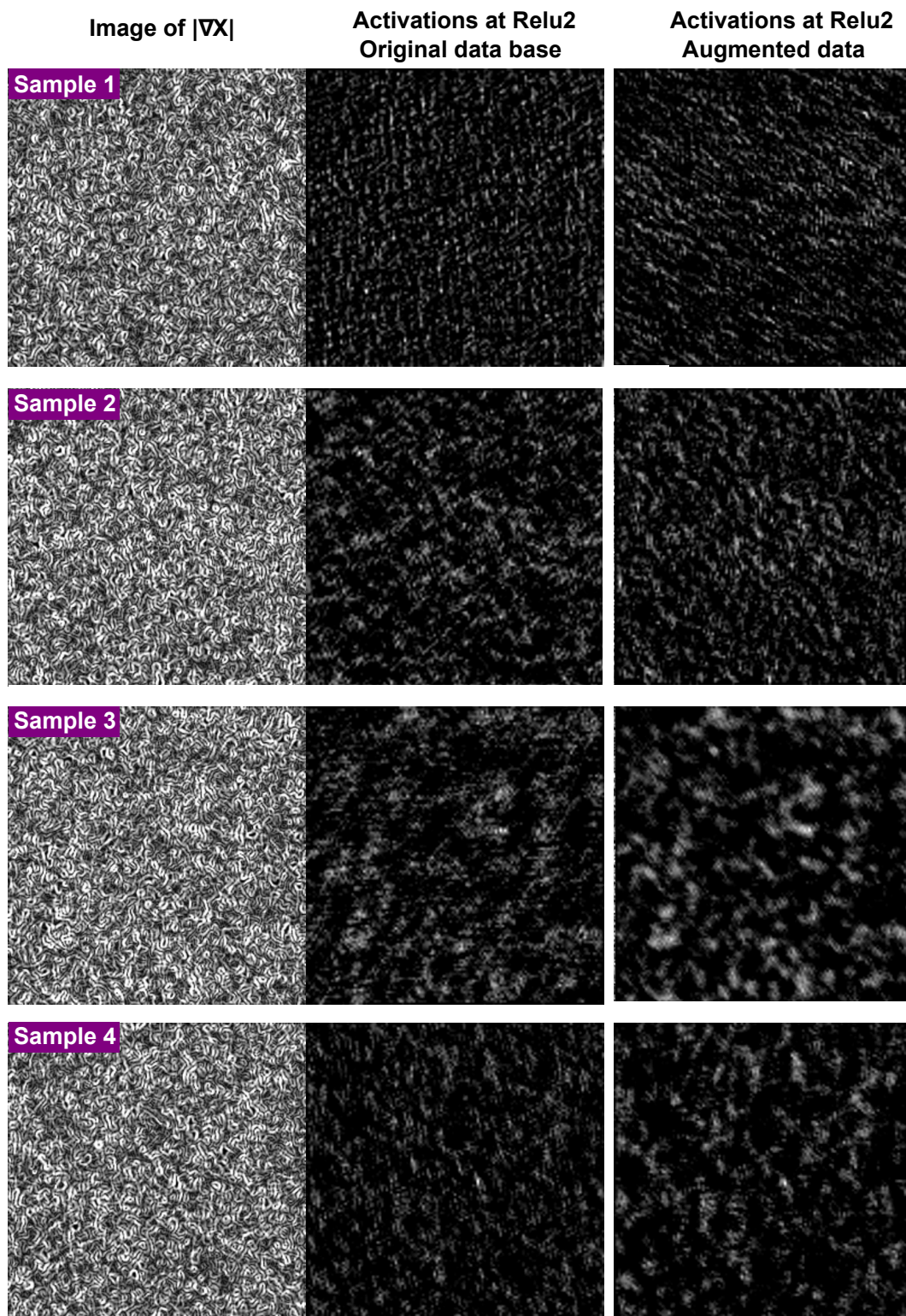


Figure 11: Inverse problem. First column shows a typical image of  $X = |\nabla Y|$  of samples 1-4 (top to bottom). Second column shows the  $\alpha$  channel at Conv2 of samples 1-4 (top to bottom) obtained using the original data base. Third column shows the  $\alpha$  channel at Conv2 of samples 1-4 (top to bottom) obtained from an augmented data base. The  $\alpha$  channel shows important features in the images for classification. Notice that the responses in sample No. 3 are notably more prominent than those in the other samples, as expected.

### 3.3 Eigenfeatures

Using the  $\alpha$  channel with the strongest activation as criterion to select the most representative features of each sample is not necessarily the best alternative available. Although this method highlights differences among the samples, the learned features at individual layers can be sensitive to the initial values of the weights in different realizations of the image classification process. While it is possible that using a data set that is large enough would help to alleviate this weakness, we propose a more robust approach.

In this section, instead of using the  $\alpha$  channel, we consider simultaneously all response maps in a convolutional layer. To discover the most representative features hidden in the response maps, one idea is to assemble a matrix containing all the response maps and then extract the most representative features of this matrix. SVD provides a convenient way to organize the response maps into hierarchically ordered contributions. We briefly describe the SVD method in the next section.

#### 3.3.1 Singular value decomposition

SVD is a machine learning tool that has extraordinary applications [35, 36, 37, 38, 39]. We are interested in analyzing a data set  $\mathbf{X} \in \mathbb{R}^{n \times m}$ .

$$\mathbf{X} = \begin{bmatrix} | & | & \dots & | \\ X_1 & X_2 & \dots & X_m \\ | & | & \dots & | \end{bmatrix} \quad (14)$$

In our case, the columns  $X_k \in \mathbb{R}^n$  are individual response maps at some layer of the CNN. We consider the activations at ReLU2. The size of the response of this layer is equal to that of the input image or  $266 \times 266$  and thus we arrange each of these responses into column vectors with  $n = 70756$  elements. Each response map has index  $i = 1, 2, \dots, m$ , with  $m$  being the total number of response maps ( $m = 128$ ) because the second convolutional layer of the CNN has 128 channels.

The SVD is a unique matrix decomposition that exist for every matrix  $\mathbf{X}$ :

$$\mathbf{X} = U\Sigma\mathcal{V}^\dagger \quad (15)$$

with  $U$  and  $\mathcal{V}$  being the left and right singular vectors, respectively. The symbol  $\dagger$  indicates transpose. The details of SVD can be found in the literature [40]. For the purpose of this work, suffice to say that SVD is a matrix factorization into unitary matrices  $U$  and  $\mathcal{V}$  with orthonormal columns that are ordered hierarchically according to their importance, and  $\Sigma$  is a diagonal matrix containing the singular values.

A convenient statistical interpretation of the SVD involves the correlation matrix  $\mathbf{X}^\dagger\mathbf{X}$  defined as

$$\mathbf{X}^\dagger\mathbf{X} = \begin{bmatrix} X_1^\dagger X_1 & X_1^\dagger X_2 & \dots & X_1^\dagger X_m \\ X_2^\dagger X_1 & X_2^\dagger X_2 & \dots & X_2^\dagger X_m \\ \dots & \dots & \dots & \dots \\ X_m^\dagger X_1 & X_m^\dagger X_2 & \dots & X_m^\dagger X_m \end{bmatrix} \quad (16)$$

where each entry  $X_i^\dagger X_j = \langle X_i, X_j \rangle$  represents the inner product between columns  $i$  and  $j$ . In other words,  $X_i^\dagger X_j$  accounts for the overlapping between all pairs of columns. This matrix accounts for the correlation between all of the response maps in  $\mathbf{X}$ .

To bring the SVD into play, notice that eqn. 15 allows us to write  $\mathbf{X}^\dagger\mathbf{X} = \mathcal{V}\Sigma^2\mathcal{V}^\dagger$ . Similarly,  $\mathbf{X}\mathbf{X}^\dagger = U\Sigma^2U^\dagger$ . These expressions can be written as the following eigenvalue problems:

$$\begin{aligned} \mathbf{X}^\dagger\mathbf{X}\mathcal{V} &= \mathcal{V}\Sigma^2 \\ \mathbf{X}\mathbf{X}^\dagger U &= U\Sigma^2 \end{aligned} \quad (17)$$

It is clear from eqn. 17 that the columns of  $\mathcal{V}$  and  $U$  are eigenvectors of the correlation matrices  $\mathbf{X}^\dagger\mathbf{X}$  and  $\mathbf{X}\mathbf{X}^\dagger$ , respectively. Loosely speaking, since the columns in  $U$  are ordered according to their importance, then the data in  $\mathbf{X}$  has its larger correlation along the  $u_1$  eigendirection. Where  $u_1$  is the first column of the left singular eigenvector  $U$ . These eigenvectors define directions along which all the feature maps in  $\mathbf{X}$  have the largest variance. In this context, the eigenvectors are the principal component directions  $\text{PC}_i$ .

### 3.3.2 Eigenvectors of the response maps

The process of feature discovery of a test image is summarized in figure 7. To obtain the most representative features of a test image of the absolute gradient of a sample of material, firstly we feed this test image into the CNN that has been trained using the parameters shown in Table 1. Secondly, we collect all the channels containing response maps of the test image and use each response map as a column vector  $X_i$  for the matrix  $\mathbf{X}$  in eqn. 14. We then apply the SVD method to the whole library of response maps obtained at the ReLU2 layer, which follows the second convolutional layer. The fast decay of the singular values shown in Figure 7d suggests that the first eigenvector,  $u_1$  can be used to represent the most relevant features at the second convolutional layer. The eigenvector  $u_1$  represents the direction in which  $\mathbf{X}$  has the largest variance. Thus this eigenvector represents the *eigenfeatures* of a given sample.

We apply the above process to extract the eigenfeatures of typical images of samples 1-4 and the result is shown in the second column of Figure 13. Notice that the eigenfeatures are similar in appearance to the  $\alpha$  channel shown in Figure 11 from the previous section. The eigenfeatures possess the notable difference of being statistically robust in the sense that they seem to be insensitive to the initial values of the weights, which is a desired property.

It is crucial to verify that the eigenfeatures found in the samples are correct and robust. This is specially necessary because of the limited size of our data base, although we have employed augmentation to enlarge the data base. To this end, we have employed several approaches, namely weight regularization and addition of dropout to the fully-connected layer. Another technique to make sure that overfitting is not significant consists in reducing the capacity of the network [10, 41]. One way to implement this in practice is to compare models having different numbers of hidden units [8]. We assessed this idea in our model by removing the last convolutional block and additionally we substantially decreased the number of learnable parameters by halving the number of channels in each one of the first two layers, thereby leaving the first two convolutional layers with 64 channels each. Figure 12 shows the training progress of the simpler model with reduced capacity, in which we have used a mini-batch of size 32. The steady decrease of the training and validation loss, suggests that there is no significant overfitting and the final accuracy is similar to that of the original model. We observed no significant reduction in classification accuracy and more importantly, the eigenfeatures in samples 1-4 remain more or less unchanged, as shown in the third column of Figure 13.

## 4 Discussion and conclusions

A highly accurate CNN classifies images of the magnitude of the gradient of X-ray of samples of epoxy resins. The feature maps of the intermediate layers contain the most representative low-level features in a test image. The strongest activated channel produces an image of these features providing us with a simple visual summary of a given sample. However different realizations of the classification process result in slightly different features. For images with well-defined segments, such as faces or objects, this method can be considered adequate. In the case of X-ray images of resins, the descriptive features are distributed throughout the whole domain and therefore a better visualization of the representative features is desirable.

SVD provides a means to expand a matrix of feature maps,  $\mathbf{X}$ , in terms ordered hierarchically as:

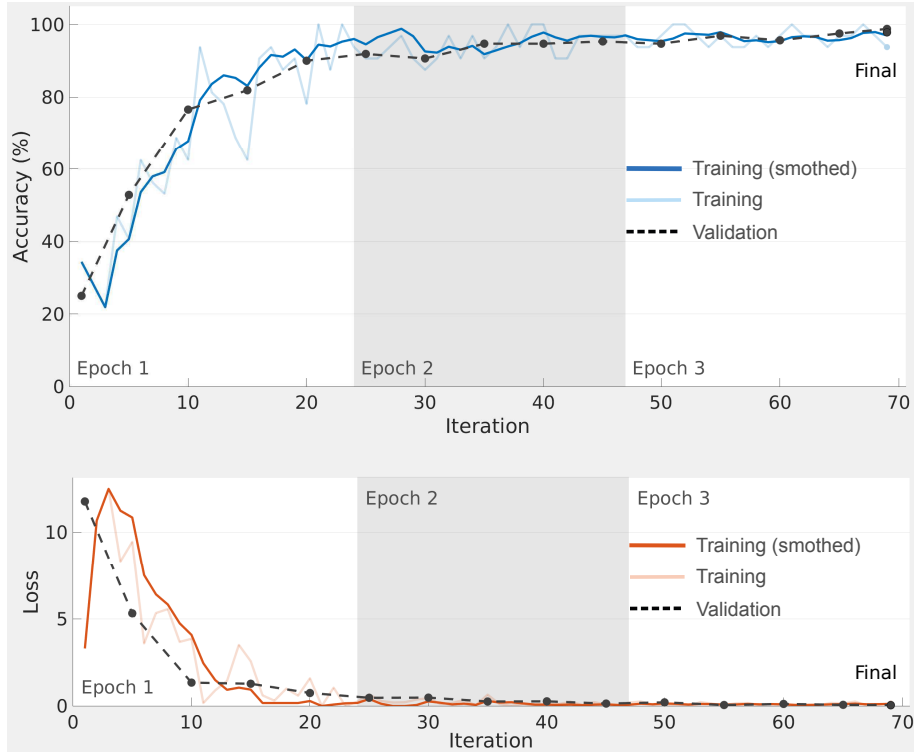


Figure 12: Training progress of the CNN with reduced capacity using the hyperparameters described in the text. Using a mini-batch size of 32, it takes 23 iterations to all of the training samples pass through the learning algorithm. (a) Training and validation accuracy reaches more or less the same high values after 70 iterations. (b) The steady decrease of the training and validation loss functions suggests that there is not significant overfitting.

$$\mathbf{X} = \sigma_1 u_1 v_1^\dagger + \sigma_2 u_2 v_2^\dagger + \dots + \sigma_m u_m v_m^\dagger \quad (18)$$

Truncating the sum in eqn. 18 to include only the first  $r$  terms results in the matrix  $\tilde{\mathbf{X}} = \tilde{U}\tilde{\Sigma}\tilde{V}^\dagger$ . The Eckard-Young theorem [42] guarantees that the best approximation to  $\mathbf{X}$  of rank- $r$  is  $\tilde{\mathbf{X}}$ , according to

$$\arg \min_{\tilde{\mathbf{X}} \text{ s.t. } \text{rank}(\tilde{\mathbf{X}})=r} \|\mathbf{X} - \tilde{\mathbf{X}}\|_F = \tilde{U}\tilde{\Sigma}\tilde{V}^\dagger \quad (19)$$

Where  $\|\cdot\|_F$  is the Frobenius norm. Then the best approximation to  $\mathbf{X}$  that has rank  $r = 1$  is given by

$$\tilde{\mathbf{X}} = \sigma_1 u_1 v_1^\dagger \quad (20)$$

Where  $u_1$  is the first column in the left singular eigenvector which has the same size as the response maps  $X_i$ . Therefore, the eigenfeatures vector is an optimal representation of the rank-1 truncation of the whole library of response maps and contains the most representative features of the original test image of a given sample.

Some advantages of proposed approach are the following: (i) The eigenfeatures are in agreement with the results obtained using the strongest activated channel. This means that both methods highlight approximately the same region in the domain of the test image, although the eigenfeatures appear to have a much clear appearance than the features in the strongest activation channel. (ii) The eigenfeatures are statistically robust in the sense that they remain unchanged when retraining the CNN with different initial values of the weights. (iii) More importantly, the eigenfeatures seem to be statistically robust across different network architectures.

To demonstrate this, we retrained the AlexNet [7] to classify 4 samples of materials. We then used the SVD-based approach to summarize the response maps and observed that the resulting eigenfeatures have similar appearance to what is shown in figure Figure 13.

The SVD-based method to extract the most representative features of an X-ray image can be appropriate to a large variety of applications, including polymers, metal alloys, among others. Since opposite signs of  $u_1$  represent the same eigenvector, a future work should focus on developing an unsupervised selection of the correct sign of the eigenfeatures.

## References

- [1] S.C. Garcea, Y. Wang, and P.J. Withers. X-ray computed tomography of polymer composites. *Composites Science and Technology*, 156:305 – 319, 2018.
- [2] Edgar Avalos, Shuangquan Xie, Kazuto Akagi, and Yasumasa Nishiura. Bridging a mesoscopic inhomogeneity to macroscopic performance of amorphous materials in the framework of the phase field modeling. *Physica D: Nonlinear Phenomena*, 409:132470, 2020.
- [3] Yann LeCun, Yoshua Bengio, and Geoffrey Hinton. Deep learning. *Nature*, 521:436 EP –, May 2015.
- [4] Guangzhou An, Kazuko Omodaka, Satoru Tsuda, Yukihiro Shiga, Naoko Takada, Tsutomu Kikawa, Toru Nakazawa, Hideo Yokota, and Masahiro Akiba. Comparison of machine-learning classification models for glaucoma management. *J Healthc Eng*, 2018:6874765, Jun 2018. 30018755[pmid].
- [5] Jonathan Schmidt, Mário R. G. Marques, Silvana Botti, and Miguel A. L. Marques. Recent advances and applications of machine learning in solid-state materials science. *npj Computational Materials*, 5(1):83, 2019.
- [6] Y. LeCun. Generalization and network design strategies. In R. Pfeifer, Z. Schreter, F. Fogelman, and L. Steels, editors, *Connectionism in Perspective*, Zurich, Switzerland, 1989. Elsevier. an extended version was published as a technical report of the University of Toronto.
- [7] Alex Krizhevsky, Ilya Sutskever, and Geoffrey E. Hinton. Imagenet classification with deep convolutional neural networks. In *Proceedings of the 25th International Conference on Neural Information Processing Systems - Volume 1*, NIPS’12, pages 1097–1105, USA, 2012. Curran Associates Inc.
- [8] Christopher M. Bishop. *Neural Networks for Pattern Recognition*. Oxford University Press, Inc., New York, NY, USA, 1995.
- [9] Matthew D. Zeiler and Rob Fergus. Visualizing and understanding convolutional networks. In David Fleet, Tomas Pajdla, Bernt Schiele, and Tinne Tuytelaars, editors, *Computer Vision – ECCV 2014*, pages 818–833, Cham, 2014. Springer International Publishing.
- [10] Francois Chollet. *Deep learning with Python*. Manning Publications Co., 2018.
- [11] Angelo Ziletti, Devinder Kumar, Matthias Scheffler, and Luca M. Ghiringhelli. Insightful classification of crystal structures using deep learning. *Nature Communications*, 9(1):2775, 2018.
- [12] Dragan Mlakić, Srete Nikolovski, and Ljubomir Majdandžić. Deep learning method and infrared imaging as a tool for transformer faults detection. *J. of Electrical Engineering*, 6(2), March 2018.

- [13] Y. Xing, C. Lv, H. Wang, D. Cao, E. Velenis, and F. Wang. Driver activity recognition for intelligent vehicles: A deep learning approach. *IEEE Transactions on Vehicular Technology*, 68(6):5379–5390, June 2019.
- [14] Xiangyu Zhang, Jianhua Zou, Kaiming He, and Jian Sun. Accelerating very deep convolutional networks for classification and detection. *CoRR*, abs/1505.06798, 2015.
- [15] Marcella Astrid and Seung-Ik Lee. Deep compression of convolutional neural networks with low-rank approximation. *ETRI Journal*, 40(4):421–434, 2018.
- [16] Yangyang Wang, Shuzhan Huang, Juying Dai, and Jian Tang. A novel bearing fault diagnosis methodology based on SVD and one-dimensional convolutional neural network. *Shock and Vibration*, 2020:1–17, January 2020.
- [17] Rafael C. Gonzalez and Richard E. Woods. *Digital Image Processing (3rd Edition)*. Prentice-Hall, Inc., Upper Saddle River, NJ, USA, 2006.
- [18] F. Fogelman-Soulié, P. Gallinari, Y. LeCun, and S. Thiria. Automata networks and artificial intelligence. In *Automata networks in computer science, theory and applications*, pages 133–186. Princeton University Press, 1987.
- [19] Simon S. Haykin. *Neural networks and learning machines*. Pearson Education, Upper Saddle River, NJ, third edition, 2009.
- [20] Jake Bouvrie. Notes on convolutional neural networks. Technical report, Center for Biological and Computational Learning, Department of Brain and Cognitive Sciences, Massachusetts Institute of Technology, 2006. Technical report.
- [21] Sergey Ioffe and Christian Szegedy. Batch normalization: Accelerating deep network training by reducing internal covariate shift, 2015.
- [22] Kevin Jarrett, Koray Kavukcuoglu, Marc’Aurelio Ranzato, and Yann LeCun. What is the best multi-stage architecture for object recognition? In *Proc. International Conference on Computer Vision (ICCV’09)*. IEEE, 2009.
- [23] Vinod Nair and Geoffrey E. Hinton. Rectified linear units improve restricted boltzmann machines. In *Proceedings of the 27th International Conference on International Conference on Machine Learning, ICML’10*, page 807–814, Madison, WI, USA, 2010. Omnipress.
- [24] J. Nagi, F. Ducatelle, G. A. Di Caro, D. Cireşan, U. Meier, A. Giusti, F. Nagi, J. Schmidhuber, and L. M. Gambardella. Max-pooling convolutional neural networks for vision-based hand gesture recognition. In *2011 IEEE International Conference on Signal and Image Processing Applications (ICSIPA)*, pages 342–347, 2011.
- [25] Ian Goodfellow, Yoshua Bengio, and Aaron Courville. *Deep Learning*. MIT Press, 2016. <http://www.deeplearningbook.org>.
- [26] Yoshua Bengio. Practical recommendations for gradient-based training of deep architectures, 2012.
- [27] Dominic Masters and Carlo Luschi. Revisiting small batch training for deep neural networks, 2018.
- [28] N. Srivastava, G. Hinton, A. Krizhevsky, I. Sutskever, and R. Salakhutdinov. Dropout: A simple way to prevent neural networks from overfitting. *Journal of Machine Learning Research*, 15:1929–1958, 2014. cited By 9824.
- [29] Christopher Bishop. *Pattern Recognition and Machine Learning*. Springer, January 2006.

- [30] Kevin P. Murphy. *Machine learning : a probabilistic perspective*. MIT Press, Cambridge, Mass. [u.a.], 2013.
- [31] Connor Shorten and Taghi M. Khoshgoftaar. A survey on image data augmentation for deep learning. *Journal of Big Data*, 6(1):60, 2019.
- [32] M. Mohsin Jadoon, Qianni Zhang, Ihsan Ul Haq, Sharjeel Butt, and Adeel Jadoon. Three-class mammogram classification based on descriptive CNN features. *BioMed Research International*, 2017:1–11, 2017.
- [33] Dragan Mlakic, Srete Nikolovski, and Ljubomir Majdandzic. Deep learning method and infrared imaging as a tool for transformer faults detection. *Journal of Electrical Engineering*, 6:98–106, 2018.
- [34] Fred Hohman, Haekyu Park, Caleb Robinson, and Duen Horng Chau. Summit: Scaling deep learning interpretability by visualizing activation and attribution summarizations, 2019.
- [35] Trevor Hastie, Robert Tibshirani, and Jerome Friedman. *The Elements of Statistical Learning*. Springer Series in Statistics. Springer New York Inc., New York, NY, USA, 2001.
- [36] J. Nathan Kutz. *Data-Driven Modeling & Scientific Computation: Methods for Complex Systems & Big Data*. Oxford University Press, Inc., New York, NY, USA, 2013.
- [37] O. Alter, P. O. Brown, and D. Botstein. Singular value decomposition for genome-wide expression data processing and modeling. *Proceedings of the National Academy of Sciences of the United States of America*, 97(18):10101–10106, Aug 2000. 10963673[pmid].
- [38] Myeongsu Kang and Jong-Myon Kim. Singular value decomposition based feature extraction approaches for classifying faults of induction motors. *Mechanical Systems and Signal Processing*, 41(1):348 – 356, 2013.
- [39] F. Fioranelli, M. Ritchie, and H. Griffiths. Classification of unarmed/armed personnel using the netrad multistatic radar for micro-doppler and singular value decomposition features. *IEEE Geoscience and Remote Sensing Letters*, 12(9):1933–1937, Sep. 2015.
- [40] Gilbert Strang. *Linear Algebra and Its Applications*. Academic Press, 1980.
- [41] Shizuo Kaji and Satoshi Kida. Overview of image-to-image translation by use of deep neural networks: denoising, super-resolution, modality conversion, and reconstruction in medical imaging. *Radiological Physics and Technology*, 12(3):235–248, 2019.
- [42] Carl Eckart and Gale Young. The approximation of one matrix by another of lower rank. *Psychometrika*, 1(3):211–218, 1936.

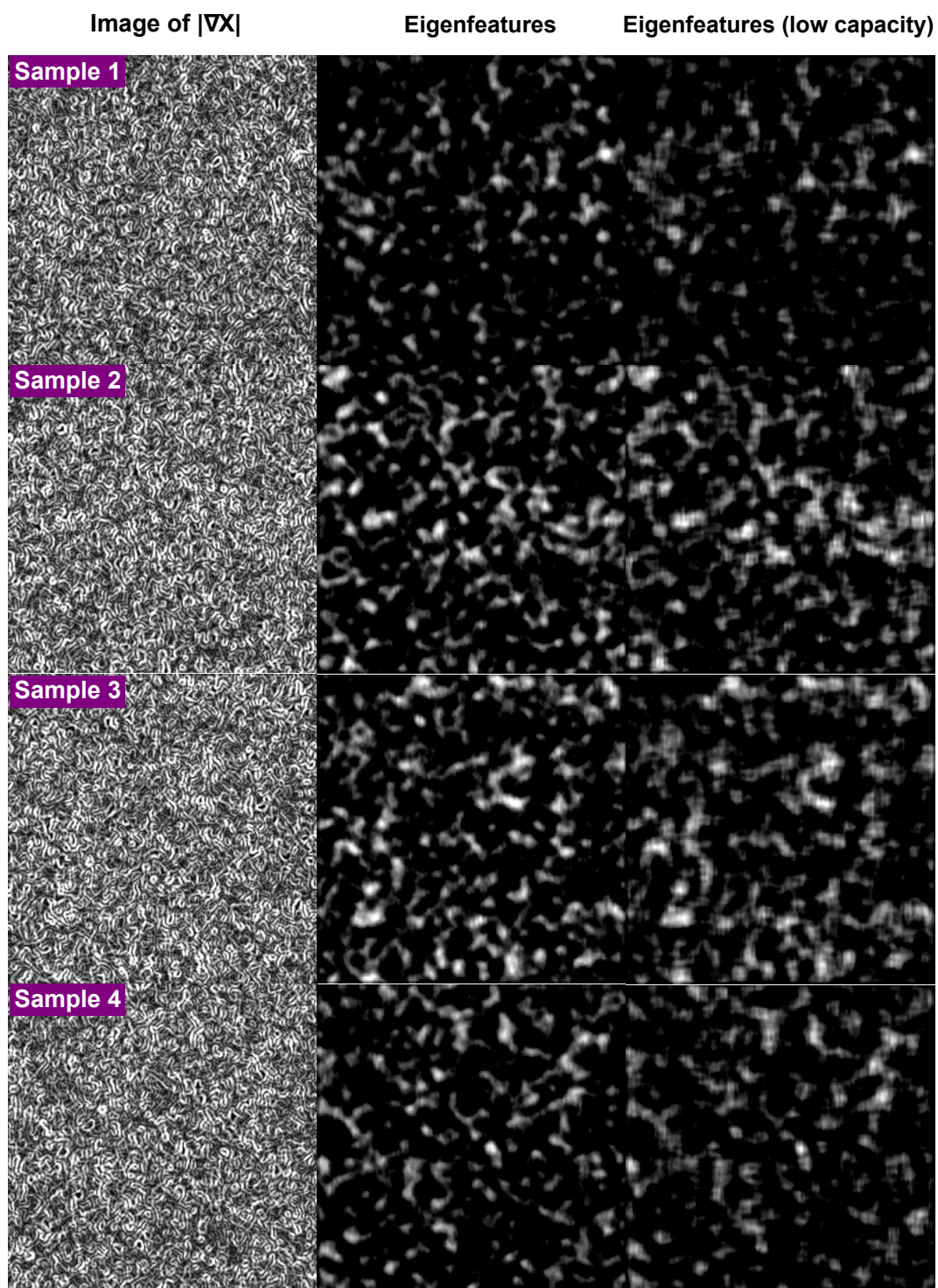


Figure 13: Eigenfeatures. First column shows a typical image of  $X$  of samples 1-4 (top to bottom). Second column shows eigenfeatures of the whole set of responses at the second convolutional layer for samples 1-4 (top to bottom). The eigenfeatures highlight differences among samples. Notice that the features in sample No. 3 are notably more prominent than those in the other samples, as expected. Third column shows eigenfeatures using a CNN of reduced capacity, as described in the text.